PHYSICAL REVIEW A **107**, 032607 (2023)

Superresolution imaging with multiparameter quantum metrology in passive remote sensing

Emre Köse [*] and Daniel Braun [†]
Institut für Theoretische Physik, Eberhard Karls Universität Tübingen, 72076 Tübingen, Germany

(Received 11 January 2023; accepted 24 February 2023; published 14 March 2023)

We study super-resolution imaging theoretically using a distant n-mode interferometer in the microwave regime for passive remote sensing, used, e.g., for satellites like the “Soil Moisture and Ocean Salinity” (SMOS) mission to observe the surface of the Earth. We give a complete quantum-mechanical analysis of multiparameter estimation of the temperatures on the source plane. We find the optimal detection modes by combining incoming modes with an optimized unitary that enables the most informative measurement based on photon counting in the detection modes and saturates the quantum Cramér-Rao bound from the symmetric logarithmic derivative for the parameter set of temperatures. In our numerical analysis, we achieved a quantum-enhanced super-resolution by reconstructing an image using the maximum likelihood estimator with a pixel size of 3 km, which is ten times smaller than the spatial resolution of SMOS with comparable parameters. Further, we find the optimized unitary for uniform temperature distribution on the source plane, with the temperatures corresponding to the average temperatures of the image. Even though the corresponding unitary was not optimized for the specific image, it still gives a super-resolution compared to local measurement scenarios for the theoretically possible maximum number of measurements.

DOI: 10.1103/PhysRevA.107.032607

I. INTRODUCTION

The technology of imaging is currently undergoing a rapid evolution both due to enhanced computational techniques [1] and due to insights from quantum information processing and quantum metrology. It has become clear that the paradigmatic resolution limit found by Abbe and Rayleigh, based on the interference of classical waves set by the wavelength of the light, is not the ultimate fundamental bound if the quantum nature of light is taken into account. In quantum optics it was realized already in the 1960s in the context of the explication of the Hanbury–Brown Twiss effect [2,3] that fundamentally the interference of light should be considered in Hilbert space and can lead to higher-order correlations that contain information beyond the first-order correlations relevant to the interference patterns of classical electromagnetic waves. Experimentally, super-resolution was demonstrated by Hell in 1994 (see Refs. [4,5]), who resolved a molecule with nanometer resolution with light in the optical domain by a decoration of the molecule with pointlike emitters and quenching them selectively. Early theoretical work used the techniques of optimal parameter estimation to estimate the ultimate sensitivities of radar and, in fact, led to the development of quantum parameter estimation theory [6–9]. Much later, quantum parameter estimation theory was applied to determine optimal detection modes and ultimate sensitivities for arbitrary parameters encoded in the quantum state of Gaussian light [10,11]. In 2016, Nair and Tsang [17] wrote a seminal paper that considered the problem of ultimate resolution as a quantum parameter estimation problem for the distance between the two sources. They found that the quantum Fisher information (QFI) that sets the ultimate bound remains finite for two point sources of low, identical intensity in the limit of vanishing separation, whereas the classical Fisher information linked to intensity measurements in direct imaging vanishes. A large amount of theoretical [12–36] and experimental research [37–42] followed that corroborated and generalized this insight.

Most of these works concentrated on estimating one or few parameters, however, typically linked to geometrical information like the spatial separation or position of point sources and, in some cases, optical phase imaging, i.e., the joint estimation of the phases with respect to a reference mode [43–46]. While this led to important insights and solid evidence that, in many situations, quantum parameter estimation techniques can enhance resolution beyond the classical diffraction limit, imaging typically does not aim at recovering information about the separation or, more generally, the spatial position of point sources. Instead, in a typical image, the scene is covered by pixels of known locations and one wants to know for each pixel the intensity of the source in that point, its spectral composition, polarization, etc. Since an image typically consists of many pixels, imaging is then inherently a (quantum) many-parameter estimation problem, and corresponding techniques should be applied to obtain the best possible image reconstruction quality based on the gathered measurement results.

In this paper, we take an important step in this direction in passive remote sensing of Earth in the micro-wave domain, building on our previous work [47]. Here, the state of the art is interferometric antenna synthesis, with which a large effective antenna can be formed from a set of small antennas, with corresponding enhanced resolution. For example, the “Soil Moisture and Ocean Salinity” (SMOS) satellite is an interferometer with a Y-shaped array of 69 antennas where

---

[*] saban-emre.koese@uni-tuebingen.de
[†] daniel.braun@uni-tuebingen.de

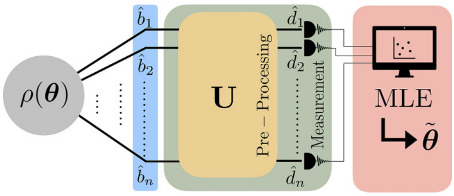

FIG. 1. The Gaussian state $\rho(\boldsymbol{\theta})$ of the n-mode interferometer contains the spatial and the radiometric information from current density sources. The incoming modes $\hat{b}_i$ are combined with an optimized $\mathbf{U}$ to have detection modes $\hat{d}_i$ of the photon counting measurement. For experimental realization, one can decompose $\mathbf{U}$ into $SU(2)$ group elements similar to optical quantum computing, i.e., using beam splitters and phase shifters. After the measurements, one estimates the parameter set using an estimator function such as a maximum likelihood estimator (MLE).

each arm has a length of around 4 m [48–51]. It achieves a resolution of about $d \simeq 35$ km, from a distance $R \simeq 758$ km above the surface of Earth by measuring the thermal noise in a narrow frequency band of electromagnetic fields (1420–1427 MHz, central wavelength $\lambda \simeq 21$ cm). The electric fields are sampled in real time, filtered, and interfered numerically, implementing thus purely classical interference. The diffraction limit analogous to the ones by Abbe and Rayleigh is given here by the van Cittert–Zernike theorem [52–54], $d \simeq \lambda R/\Delta x_{ij}$, where Δx_{ij} is the maximal spatial separation between two antennas. From the interferometric data one can, via inverse spatial Fourier transform, estimate the local brightness temperatures T_{eff} on the surface of Earth with resolution d, and from these, with appropriate models, the soil moisture and ocean salinity. This information is of great importance for the geosciences, monitoring of Earth, climate modeling, flood predictions, and much more. Driven by these applications, there is the desire to enhance the spatial resolution but simply increasing the size of the satellite becomes unpractical and lowering its orbit reduces its lifetime.

Here we show that with appropriate techniques from multiparameter quantum estimation theory, one can reconstruct images of Earth with roughly a factor 10 better spatial resolution than SMOS with a satellite of comparable size. We demonstrate this with images of up to 30 pixels, showing that they can be reconstructed faithfully with a pixel size of 3 km. Instead of local measurement of the incoming modes of the interferometer, we combine the modes with a unitary transformation that enables nonlocal measurements. We find the optimal unitary matrix that minimizes the scalar classical Cramér-Rao bound (CCRB) [55] for the classical Fisher information matrix for the chosen measurements contracted with a weight matrix. The corresponding unitary matrix can be decomposed into phase shifters and, at most, $n(n-1)/2$ beam splitters, as is well known from linear optical quantum computing [56]. This allows us to quantum program optimal measurement schemes for imaging. Contrary to classical computational imaging [1], the quantum computation for this new kind of "quantum-computational imaging" is done before the measurements (see Fig. 1).

Multiparameter quantum estimation theory is by itself a rapidly evolving field. Recently, there have been many different works, e.g., multiparameter estimation of several phases [43], estimation of all three components of a magnetic field [57], optimal estimation of the Bloch vector components of a qubit [58], multiparameter estimation from Markovian dynamics [59], etc. (see the review article [60]). For a limited sample size, like in passive sensing, it is crucial to estimate the image's parameters simultaneously. The multiparameter quantum Cramér-Rao bound (QCRB) can, in general, not be saturated. Optimal measurements linked to different parameters do not typically commute and hence lead to incompatible measurements. Once the commutation on average is satisfied, the quantum limit is asymptotically attainable [61].

We build on our previous work [47,54,62], where we showed that thermal fluctuations of the microscopic currents lead to Gaussian states of the microwave field and hence allow one to use the QCRB for Gaussian states [10,11,63,64]. As before, we assume that only the current densities at the surface of Earth contribute and neglect the cosmic microwave background as well as additional technical noises [65–67].

We organize the rest of the paper as follows. In Sec. II, we introduce the quantum state received by the n-mode interferometer, as well as the QFI, the symmetric logarithmic derivative (SLD), and the corresponding quantum Cramér-Rao lower bound. Further, we present the optimal positive operator-valued measure (POVM), which minimizes the most informative bound for the multiparameter estimation. In Sec. III, first, we discuss the simple problem as a benchmark considering two-pixel sources with the two-mode interferometer. We analyze the quantum advantage with the optimal unitary compared to local measurement scenarios. Second, we increase the number of pixels by considering a one-dimensional (1D) array of sources with a 1D array interferometer. We examine how closely we can approach the quantum limit of sensitivity with our parameter set. Third, we consider a two-dimensional (2D) source image with a 2D array interferometer. Using the maximum likelihood estimator (MLE), we reconstruct the image for the POVMs with the optimized unitary specific to the image, the optimized unitary for uniform temperature distribution, and local measurements. We conclude in Sec. IV.

II. THEORY

A. State received by the *n*-mode interferometer

In previous work [47], we analyzed the quantum state radiated from current current distribution $\mathbf{j}(\mathbf{r}, t)$ [62,68–77] on the source plane. We show that the state of the incoming modes of the n-mode interferometer from these radiated sources can be modeled as circularly symmetric Gaussian states with a partial coherence, which encodes the information of position and amplitudes distribution of the sources. Then after the scattering process [78,79] from the interferometer, the partially coherent state received in the n modes is represented by

$$\rho = \int d^{2n}\beta\, \Phi(\{\beta_i\}) |\{\beta_i\}\rangle\langle\{\beta_i\}|, \tag{1}$$

where $|\{\beta_i\}\rangle$ is a multimode coherent state for spatial antenna modes, $\{\beta_i\} = \beta_1, \beta_2, \ldots, \beta_n$, and

$$\Phi(\{\beta_i\}) = \frac{1}{\pi^n \det \Gamma} e^{-\bar{\beta}^\dagger \Gamma^{-1} \bar{\beta}}, \tag{2}$$

where $\bar{\beta}^T = (\beta_1, \beta_2, \dots, \beta_n)$ is the Sudarshan-Glauber representation, and $d^{2n}\beta \equiv d\mathrm{Re}\beta_1 d\mathrm{Im}\beta_1 \dots d\mathrm{Re}\beta_n d\mathrm{Im}\beta_n$. The matrix Γ is the coherence matrix for n antenna modes, and its elements are defined as $\Gamma_{ij} = \langle \hat{b}_i^\dagger \hat{b}_j \rangle$. Considering the sources of these fields are generated by random current distribution on the source plane and assuming that each antenna has the same polarization direction $\hat{e}_l$ and they filter incoming fields with the same frequency ω_0 with a bandwidth B, then one finds a relation between $\langle b_i^\dagger b_j \rangle$ and the average current density distribution on the source plane as [47]

$$\langle \hat{b}_i^\dagger \hat{b}_j \rangle = K \int d^3r \, \frac{\langle |\tilde{\mathcal{J}}_{t,l}(\mathbf{r}, \omega)|^2 \rangle \, e^{i\omega_0(|\mathbf{r}-\mathbf{r}_j|-|\mathbf{r}-\mathbf{r}_i|)/c}}{|\mathbf{r} - \mathbf{r}_i||\mathbf{r} - \mathbf{r}_j|} \times \mathrm{sinc}\left[\frac{B}{2c}(|\mathbf{r} - \mathbf{r}_j| - |\mathbf{r} - \mathbf{r}_i|)\right], \tag{3}$$

where d^3r is the integral over the source volume, $\mathbf{r}_i$ is the location of the detector for received modes in the detection plane, and $\mathrm{sinc}(x) = \sin(x)/x$. $\tilde{\mathcal{J}}_{t,l}(\mathbf{r}, \omega)$ is the Fourier transform of the locally transverse component of the current density $\boldsymbol{\mathcal{J}}(\mathbf{r}, t)$ and l stands for the component parallel to the source plane. Considering R as the distance between source and detection planes, we can parametrize the integral over Earth's surface as $\mathbf{r} = (x, y, R)$ with respect to the coordinate system of the detection plane. Assuming that we are in the far-field regime $|\Delta\mathbf{r}_{ij}| \ll R$, where $\Delta\mathbf{r}_{ij} = \mathbf{r}_j - \mathbf{r}_i$ is the distance between two antennas, we approximate $|\mathbf{r} - \mathbf{r}_j| - |\mathbf{r} - \mathbf{r}_i| \approx \Delta\mathbf{r}_{ij} \cdot \mathbf{r}/|\mathbf{r}|$. In the denominator, we approximate $|\mathbf{r} - \mathbf{r}_i| \approx R/\cos\tilde{\theta}(x, y)$ with $\tilde{\theta}(x, y)$ the polar angle between the z axis and the vector (x, y, R). We find the relation of the average amplitude of current density distribution to brightness temperature as $T_\mathrm{B}(x, y)$ by $\langle |\tilde{\mathcal{J}}_{t,i}(\mathbf{r}, \omega)|^2 \rangle = K_1 T_\mathrm{B}(x, y) \cos\tilde{\theta}(x, y)\delta(z - R)$, where $K_1 = 32\tau_c k_B/(3l_c^3 \mu_0 c)$. Further, one can define the effective temperature as $T_\mathrm{eff}(x, y) \equiv T_\mathrm{B}(x, y) \cos^3\tilde{\theta}(x, y)$. We include an extra constant prefactor μ for the additional losses, which can be justified by tracing out modes of losses $\hat{c}$ into which photons might scatter by writing $\hat{b} = \sqrt{\mu}\hat{\tilde{b}} + \sqrt{1-\mu}\hat{c}$. Compared to the actual physical temperature, the brilliance temperature is additionally modified by the albedo of the surface from which important information, such as the surface's water content or the ocean water's salinity, can be extracted. For simplicity, we work with the physical temperatures in the following, i.e., set $T_B(x, y) = T(x, y)$. Following these assumptions and dropping the $\sim$ from $\hat{\tilde{b}}$, we simplify Eq. (3) as

$$\langle \hat{b}_i^\dagger \hat{b}_j \rangle = \frac{\mu\kappa}{R^2} \int dxdy \, T_\mathrm{eff}(x, y) e^{2\pi i(v_x^{ij} x + v_y^{ij} y)}. \tag{4}$$

We introduced a new constant $\kappa = K_1 K \equiv 2k_B/(\pi\hbar\omega_0)$ where κ has the dimension of inverse temperature with SI units (1/K) and $v_y^{ij} = \Delta x_{ij}/(\lambda R)$, $v_x^{ij} = \Delta y_{ij}/(\lambda R)$ with $\omega_0/c = 2\pi/\lambda$. Considering the parameters of SMOS, we find $\kappa = 9.4$ 1/K. The SMOS has a Y shape where each arm has a length of almost 4 m. Therefore, it is reasonable to set maximum baselines $\Delta x_\mathrm{max} = \Delta y_\mathrm{max}$ around 10 m.

B. Estimation theory of the sources

1. *Quantum Cramér-Rao bound*

For a quantum state $\rho_{\boldsymbol{\theta}}$ that depends on a vector of l parameters $\boldsymbol{\theta} = (\theta_1, \theta_2, \dots, \theta_l)^T$, an ultimate lower bound of an unbiased estimator of the parameter set is given by the quantum Cramér-Rao bound (CRB), which states that the covariance matrix of any such estimator is equal to or greater than the inverse of the QFI matrix (in the sense that their difference is a positive-semidefinite matrix). The CCRB from measurement is lower bounded by the QCRB [6,7,60] given by

$$\mathrm{Cov}(\tilde{\boldsymbol{\theta}}) \geqslant \mathscr{F}(\boldsymbol{\theta})^{-1}, \quad \mathscr{F}_{ij}(\boldsymbol{\theta}) = \tfrac{1}{2}\mathrm{Tr}(\rho_{\boldsymbol{\theta}}\{\mathscr{L}_i, \mathscr{L}_j\}), \tag{5}$$

where $\mathrm{Cov}(\tilde{\boldsymbol{\theta}})$ is a covariance matrix for the locally unbiased estimator $\tilde{\boldsymbol{\theta}}$ [61,80], the $\{\cdot, \cdot\}$ means the anticommutator, and $\mathscr{L}_i$ is the SLD related to parameter i, which is defined similarly to the single parameter case, $\frac{1}{2}(\mathscr{L}_i\rho_{\boldsymbol{\theta}} + \rho_{\boldsymbol{\theta}}\mathscr{L}_i) = \partial_i\rho_{\boldsymbol{\theta}}$. The SLD and the elements of the QFI matrix are given in Ref. [81] for any Gaussian state. The SLD can be written as

$$\mathscr{L}_i = \tfrac{1}{2}\mathfrak{M}^{-1}_{\alpha\beta,\gamma\delta}(\partial_i\Sigma^{\gamma\delta})(\mathbf{b}^\alpha\mathbf{b}^\beta - \Sigma^{\alpha\beta}), \tag{6}$$

where $\mathfrak{M}^{-1}_{\alpha\beta,\gamma\delta}$ is the fourth-order tensor form of the inverse of the matrix $\mathfrak{M} \equiv \Sigma \otimes \Sigma + \frac{1}{4}\Omega \otimes \Omega$, with $\Omega = \bigoplus_{k=1}^n i\sigma_y$, and the summation convention is used for repeated indices. In our case, the mean displacement of the Gaussian state is zero. Covariance matrix elements are given by $\Sigma^{\alpha\beta} = \frac{1}{2}\mathrm{Tr}[\rho(\mathbf{b}^\alpha\mathbf{b}^\beta + \mathbf{b}^\beta\mathbf{b}^\alpha)]$, with $\mathbf{b} = [b_1, b_1^\dagger, b_2, b_2^\dagger, \dots, b_n, b_n^\dagger]$ [10,81–85]. Then the elements of the QFI matrix in [81] become

$$\mathscr{F}_{ij} = \tfrac{1}{2}\mathfrak{M}^{-1}_{\alpha\beta,\gamma\delta}\partial_j\Sigma^{\alpha\beta}\partial_i\Sigma^{\gamma\delta}. \tag{7}$$

Using the properties of the Gaussian state (circularly symmetric and with zero mean) we can write the SLD for n mode interferometers as [47]

$$\mathscr{L}_i = \sum_j^n g_i^j \hat{b}_j^\dagger \hat{b}_j + \sum_{j<k}^n \left[g_i^{jk}\hat{b}_j^\dagger\hat{b}_k + (g_i^{jk})^*\hat{b}_k^\dagger\hat{b}_j\right] + C, \tag{8}$$

where C is a constant term that can be dropped for diagonalization purposes. In the single parameter case, the optimal POVM is the set of projectors onto eigenstates of $\mathscr{L}_i$. It allows one to saturate the QCRB in the limit of infinitely many measurements using maximum likelihood estimation [6,86,87]. To find the POVMs from the SLD, we construct a Hermitian matrix $\mathbf{M}_i$ whose diagonal elements are real-valued functions which are defined as $g_i^j \equiv \mathfrak{M}^{-1}_{\alpha\beta,\gamma\delta}(\partial_i\Sigma^{\gamma\delta})$ with $\alpha = 2j$ and $\beta = 2j - 1$. The off-diagonal elements are complex-valued functions and defined as $g_i^{jk} = \mathfrak{M}^{-1}_{\alpha\beta,\gamma\delta}(\partial_i\Sigma^{\gamma\delta})$ with $\alpha = 2j$ and $\beta = 2k - 1$ and $k > j$. By introducing a new set for the field operators such that $\bar{\mathbf{b}}^\dagger \equiv [\hat{b}_1^\dagger, \hat{b}_2^\dagger, \dots, \hat{b}_n^\dagger]$ and $\bar{\mathbf{b}} \equiv [\hat{b}_1, \hat{b}_2, \dots, \hat{b}_n]^T$, we write the SLD in the following form:

$$\mathscr{L}_i = \bar{\mathbf{b}}^\dagger\mathbf{M}_i\bar{\mathbf{b}}. \tag{9}$$

As $\mathbf{M}_i$ is a Hermitian matrix it can be unitarily diagonalized by $\mathbf{M}_i = \mathbf{V}_i^\dagger\mathbf{D}_i\mathbf{V}_i$ with $\mathbf{V}_i^\dagger\mathbf{V}_i = \mathbb{I}$. A new set of operators can be defined as $\bar{\mathbf{d}}_i^\dagger = \bar{\mathbf{b}}^\dagger\mathbf{V}_i^\dagger$ where $\bar{\mathbf{d}}_i^\dagger = [\hat{d}_{i1}^\dagger, \hat{d}_{i2}^\dagger, \dots, \hat{d}_{in}^\dagger]$. The optimal POVM for the single parameter case ($i = 1$, which we drop in the following) can be found as a set of projectors in the Fock basis $\{|m_1, m_2, \dots, m_n\rangle \langle m_1, m_2, \dots, m_n|\}_{\{m_1,m_2,\dots,m_n\}}$ of the $\hat{d}_l$ with $\hat{d}_l^\dagger \hat{d}_l |m_1, m_2, \dots, m_n\rangle = m_l |m_1, m_2, \dots, m_n\rangle$, where $l \in \{1, \dots, n\}$. The $\hat{d}_l$ will be called "detection modes." By introducing a positive weight matrix $\boldsymbol{w}$, one can define the scalar inequalities from the matrix valued QCRB as $\mathrm{Tr}[\boldsymbol{w}\,\mathrm{Cov}(\tilde{\boldsymbol{\theta}})] \geqslant \mathrm{Tr}(\boldsymbol{w}\mathscr{F}(\boldsymbol{\theta})^{-1}) \equiv C^S(\boldsymbol{\theta}, \boldsymbol{w})$. Contrary to the single parameter case, the multiparameter QCRB can generally not be saturated. Holevo realized this problem and proposed a tighter and more fundamental bound [88] $C^H(\boldsymbol{\theta}, \boldsymbol{w})$, which is upper bounded by $2C^S(\boldsymbol{\theta}, \boldsymbol{w})$ [55,89]. If the SLD operators for different parameters commute on average $\mathrm{Tr}(\rho_{\boldsymbol{\theta}}[L_i, L_j]) = 0$, then the Holevo-CRB is equivalent to the QCRB, and the QCRB for multiparameter estimation can be saturated asymptotically with a collective measurement in the limit of an infinitely large number of copies $\rho_{\boldsymbol{\theta}}^{\otimes N}$ [55,61]. The standard deviation of the estimator decreases proportionally to $1/\sqrt{N}$ for the sample size of N. The SMOS satellite travels at a constant speed of around $v \simeq 7$ km/s. It takes time $\tau = L/v$ to fly at a distance L. Each sample has a lower bound for the detection time given by $t_D \simeq 1/B$. In practice, the practical detection time might be much larger due to, e.g., deadtimes of the sensors, slow electronics, etc. In addition, zero temperature of the detector and modes $\hat{b}_i$ is implicitly assumed in our calculations but would require cooling down to temperatures much smaller than $\hbar\omega_0$. If the actual detection time is t_D^{eff}, the maximum sample size becomes $N = \tau/t_D^{\mathrm{eff}}$.

2. *Most informative bound for multiparameter metrology*

The most informative bound minimizes the classical scalar Cramér-Rao bound over all the possible POVMs. In the single parameter case, from the diagonalization of the SLD, we see that one needs to combine the incoming modes with a unitary transformation to saturate the QCRB single parameter case. This transformation, even for a single parameter, depends on the parameter itself. In the multiparameter case, any of these specific unitary transformations for a specific parameter usually gives a more significant mean-square error for the remaining parameters. Using the clue from the SLD structure, we drop the index i from the unitary transformation of the modes and minimize the scalar bound of the classical Fisher information matrix for multiparameter estimation over all possible unitaries. Then, a new set of operators for the detection modes can be defined as $\bar{\mathbf{d}} = \mathbf{U}\bar{\mathbf{b}}$ where $\bar{\mathbf{d}}^T = [\hat{d}_1, \hat{d}_2, \dots, \hat{d}_n]$, where $\mathbf{U}$ is the corresponding unitary transformation of the field modes. The average values of the elements of the new coherence matrix $\tilde{\Gamma}$ can be found by using $\hat{d}_i = \sum_l U_{il}\hat{b}_l$ as

$$\tilde{\Gamma}_{ij} = \langle d_i^\dagger d_j \rangle = \sum_{kl} U_{ik}^* U_{jl} \langle b_k^\dagger b_l \rangle. \tag{10}$$

Then we will have the probabilities after measurement $P(m_1, ..m_n|\theta_1, \theta_2, \dots, \theta_l)$ as

$$\begin{aligned} P(\{m_k\}|\boldsymbol{\theta}) &= \int d^{2n}\delta \tilde{\Phi}(\{\delta_i\}) |\langle \{m_k\}|\{\delta_i\}\rangle|^2 \\ &= \int d^{2n}\delta \tilde{\Phi}(\{\delta_i\}) \prod_i e^{-|\delta_i|^2} \frac{|\delta_i|^{2m_i}}{m_i!}, \end{aligned} \tag{11}$$

where $|\{\delta_i\}\rangle$ is a coherent state of the detection modes and $\tilde{\Phi}(\{\delta_i\})$ is the Sudarshan-Glauber function for the state of the detection modes. Due to the linear transformation from $\bar{\mathbf{b}}$ to $\bar{\mathbf{d}}$, it is still a Gaussian. It is difficult to evaluate the integral of $P(\{m_k\}|\boldsymbol{\theta})$ for all possible values of m_k and keep track of all possible combinations of photon number counts, both numerically and experimentally. Hence, instead of considering projections on the complete Fock basis as POVMs, we choose the POVMs with at most one photon per measurement and limit ourselves to $\sum_k m_k \leqslant 1$. Clearly, the resulting information loss is negligible for light that, from the very beginning, is very faint, with at most one photon per mode. However, it can be important for stronger light sources, for which one should try to resolve the photon numbers. We have the order of ten photons per mode for thermal microwave sources at room temperature. We see below that even without resolving their number, we can already largely surpass the classical resolution limit, but there is room for further improvement by going beyond the single-photon detection scheme we analyze in the following.

The selected POVM elements of single-photon detection are

$$\begin{aligned} \Pi_0 &= |0, 0, \dots, 0\rangle \langle 0, 0, \dots, 0|, \\ \Pi_k &= |0, 0, \dots, 1_k, \dots, 0\rangle \langle 0, 0, \dots, 1_k, \dots, 0|, \\ \Pi_{n+1} &= \mathbb{I} - \sum_{l=0}^{n} \Pi_l, \end{aligned} \tag{12}$$

where the last element $(n+1)$ ensures $\sum_{l=0}^{n+1} \Pi_l = \mathbb{I}$. The measurement probability of no photon in any interferometer mode becomes

$$\begin{aligned} P_0(\boldsymbol{\theta}) &= \frac{1}{\pi^n \det \tilde{\Gamma}} \int d^{2n}\delta e^{-\boldsymbol{\delta}^\dagger(\tilde{\Gamma}^{-1}+\mathbb{I})\boldsymbol{\delta}} \\ &= \frac{1}{\det(\tilde{\Gamma} + \mathbb{I})}. \end{aligned} \tag{13}$$

The single-photon detection probabilities in each mode of the interferometer follow as

$$\begin{aligned} P_k(\boldsymbol{\theta}) &= \frac{1}{\pi^n \det \tilde{\Gamma}} \int d^{2n}\delta e^{-\boldsymbol{\delta}^\dagger(\tilde{\Gamma}^{-1}+\mathbb{I})\boldsymbol{\delta}} |\delta_k|^2 \\ &= \frac{[(\tilde{\Gamma}^{-1} + \mathbb{I})^{-1}]_{kk}}{\det(\tilde{\Gamma} + \mathbb{I})}. \end{aligned} \tag{14}$$

The probability to find more than a single photon per measurement can be found as

$$P_{n+1}(\boldsymbol{\theta}) = \mathbb{I} - \sum_{k=0}^{n} P_k. \tag{15}$$

We also show the first derivative of the probability distributions of no photon detection from measurements analytically to be given by

$$\frac{\partial P_0(\boldsymbol{\theta})}{\partial \theta_i} = \left(\frac{1}{\det(\tilde{\Gamma} + \mathbb{I})}\right) \mathrm{Tr}\left(-(\tilde{\Gamma} + \mathbb{I})^{-1} \frac{\partial \tilde{\Gamma}}{\partial \theta_i}\right). \tag{16}$$

The first derivative for at most single-photon detection for all modes becomes

$$\frac{\partial P_k(\boldsymbol{\theta})}{\partial \theta_i} = \left(\frac{1}{\det(\tilde{\Gamma}+\mathbb{I})}\right) \times \left\{ \left[(\tilde{\Gamma}^{-1}+\mathbb{I})^{-1}\tilde{\Gamma}^{-1}\frac{\partial \tilde{\Gamma}}{\partial \theta_i}\tilde{\Gamma}^{-1}(\tilde{\Gamma}^{-1}+\mathbb{I})^{-1}\right]_{kk} - [(\tilde{\Gamma}^{-1}+\mathbb{I})^{-1}]_{kk}\,\mathrm{Tr}\left((\tilde{\Gamma}+\mathbb{I})^{-1}\frac{\partial \tilde{\Gamma}}{\partial \theta_i}\right)\right\}. \tag{17}$$

Finally, using Eqs. (13)–(17), the elements of the classical Fisher information can be found from

$$\mathcal{F}_{ij} = \sum_{l}^{n+1} \frac{1}{P_l(\boldsymbol{\theta})}\frac{\partial P_l(\boldsymbol{\theta})}{\partial \theta_i}\frac{\partial P_l(\boldsymbol{\theta})}{\partial \theta_j}. \tag{18}$$

The most informative bound [55] in this case is the bound minimized over all possible unitary matrices:

$$\mathrm{Tr}[\boldsymbol{w}\,\mathrm{Cov}(\tilde{\boldsymbol{\theta}})] \geqslant \min_{\mathbf{U}}\{\mathrm{Tr}[\boldsymbol{w}\mathcal{F}^{-1}(\boldsymbol{\theta})]\}. \tag{19}$$

The weight matrix is a positive definite matrix to satisfy the scalar Cramér-Rao bound. For simplicity, we consider $\boldsymbol{w} = \mathbb{I}$ to optimize the average variance of all parameters. One can also consider a diagonal matrix with different weights. This will result in directly decreasing the variances of preferred estimators. Further, choosing a weight matrix with off-diagonal elements includes covariances of the estimators. Since we assume spatially uncorrelated currents, we focus here for simplicity on the temperatures, with equal weight, rather than their correlations, which is also a preferred choice in the literature (see Ref. [55]).

3. *Maximum likelihood estimation*

Maximum likelihood estimators are widely used in estimation theory and play an essential role in interpreting the Cramér-Rao theorem [90,91]. One can estimate the set of parameters with a given probability distribution with some observed data. The likelihood function is given by $l(\boldsymbol{\theta}) = \prod_k^{n+1}(P_k(\boldsymbol{\theta}))^{N_k}$, where the total number of samples is given by $N = \sum_k^{n+1} N_k$ with N_k realizations of outcome k. Since the logarithm is a monotonously increasing function, the log of the likelihood function is maximized by the same parameter vector $\boldsymbol{\theta}$. Thus, the MLE $\hat{\boldsymbol{\theta}}_{\mathrm{MLE}}$ is a value of $\boldsymbol{\theta}$ that maximizes the log likelihood $\mathcal{L}(\boldsymbol{\theta}) = \ln[l(\boldsymbol{\theta})]$,

$$\hat{\boldsymbol{\theta}}_{\mathrm{MLE}} = \arg\max_{\boldsymbol{\theta}\in\Theta} \mathcal{L}(\boldsymbol{\theta}), \tag{20}$$

where the max is taken over the entire parameter space Θ. For sufficiently large sample size, $N \to \infty$, $\hat{\boldsymbol{\theta}}_{\mathrm{MLE}}$ converges to the true value of the parameter set $\boldsymbol{\theta}$.

III. RESULTS: ESTIMATION OF SOURCE TEMPERATURES

In this paper, our purpose is to estimate the function $T(x, y)$. Equation (4) allows us to study any source distribution on the source plane. For that aim, we partition the electromagnetic field's source on Earth's surface into square pixels of size a and effective pixel temperature T_i, located under the interferometer in the x, y plane at a distance R from the satellite. Thus, we are interested in estimating the temperature distribution in the form

$$T_{\mathrm{eff}}(x, y) = \sum_i T_i \mathrm{Box}(x - x_i, y - y_i), \tag{21}$$

where $\mathrm{Box}(x, y)$ is defined as

$$\mathrm{Box}(x, y) \triangleq \begin{cases} 1 & |x| \leqslant \frac{a}{2} \quad \text{and} \quad |y| \leqslant \frac{a}{2} \\ 0 & \text{else} \end{cases}. \tag{22}$$

Of course, this is a choice to simplify our problem to a limited number of parameters. One could also describe $T(x, y)$ using different temperature distribution functions such as Gaussian and define the parameter set according to this choice. Further, we estimate the effective pixel temperatures T_i, assuming that all the other parameters are known to a sufficiently large precision. The diagonal elements of the coherence matrix (Γ) of Gaussian states become

$$\langle \hat{b}_k^\dagger \hat{b}_k \rangle = \frac{\mu\kappa a^2}{R^2}\sum_i^p T_i, \tag{23}$$

and the off-diagonal elements are

$$\langle \hat{b}_k^\dagger \hat{b}_l \rangle = \frac{\mu\kappa a^2 \eta_{kl}}{R^2}\sum_i^p T_i e^{2\pi i (v_{kl}^x x_i + v_{kl}^y y_i)}, \tag{24}$$

where $k \neq l$ and we defined $\eta_{kl} \equiv \mathrm{sinc}(v_{kl}^x a)\,\mathrm{sinc}(v_{kl}^y a)$. The number of pixels along the $\hat{x}$ and $\hat{y}$ axis is p_x and p_y, respectively, and the number of detection modes along these axes is n_x and n_y, respectively. In total, we have $p = p_x p_y$ pixels on the surface and $n = n_x n_y$ detectors in the detection plane, of which each measures one detection mode. We set the number of detection modes equal to the number of pixels in the source plane, $n = p$, to leave no redundant parameter for the estimation, and use $n_x = p_x$ and $n_y = p_y$.

A. Resolution of two pixel sources

Let us start with two pixels (pixel 1 and pixel 2) with temperatures T_1 and T_2 in the source plane with pixel size a. Our goal is to estimate the temperatures of each source. We set the central locations of these two sources in the source plane to $(-a/2, 0, R)$ and $(a/2, 0, R)$, i.e., both are on an axis parallel to the $\hat{x}$ axis without any distance between them. In the detection plane, we have two detection modes $\hat{d}_1$ and $\hat{d}_2$ with detectors centered at positions $(-\Delta x/2, 0, 0)$ and $(\Delta x/2, 0, 0)$ on the $\hat{x}$ axis, respectively. In our previous work [47], we showed that if the mean photon numbers in each received mode of the two-mode interferometer, with circular symmetric Gaussian state, are identical ($\langle b_1^\dagger b_1\rangle = \langle b_2^\dagger b_2\rangle$), then the SLDs for T_1 and T_2 commute on average $\mathrm{Tr}(\rho_{\boldsymbol{\theta}}[L_i, L_j]) = 0$. Thus the QCRB and Holevo-CRB are equivalent: $C^S(\boldsymbol{\theta}, \boldsymbol{w}) \equiv C^H(\boldsymbol{\theta}, \boldsymbol{w})$. For each parameter, the matrix $\mathbf{M}_i$ from the SLD with $i \in \{T_1, T_2\}$ is of the form

$$\mathbf{M}_i = \begin{bmatrix} g_1^i & |g_2^i|e^{i\phi_i} \\ |g_2^i|e^{-i\phi_i} & g_1^i \end{bmatrix}, \tag{25}$$

where the ϕ_i, in general, depend on both T_1 and T_2. The ϕ_1 and ϕ_2 differ for single parameter estimation of T_1 and T_2. The

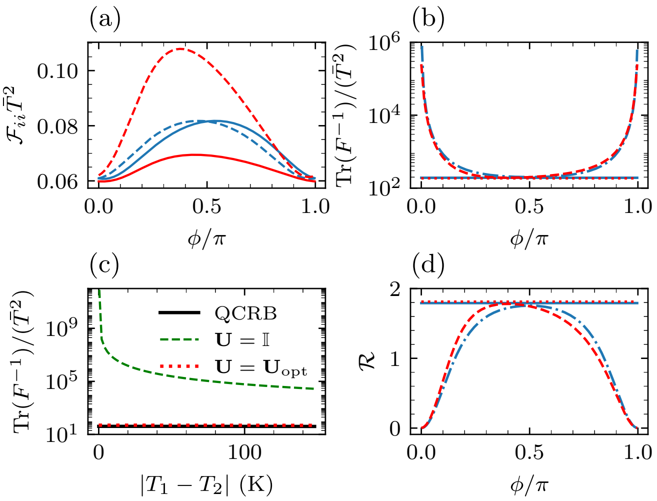

FIG. 2. Temperature estimation of two pixels. (a) The diagonal elements of the Fisher information matrix (dimensionless) as a function of ϕ. The dashed curves are for $\mathcal{F}_{T_1}$, and solid curves are for $\mathcal{F}_{T_2}$. (b) The scalar CRBs as a function of ϕ scaled with the average temperature $\bar{T}$ square of the sources. The flat lines are for the QCRBs, and the others are the CCRBs for the measurement. (c) The scalar CRBs as a function of the temperature difference of two pixels. Solid black is for QCRB, red dotted is for CCRB for optimized ϕ, and the green dashed curve is for the scalar CCRB for local measurement considering $\mathbf{U} = \mathbb{I}$. (d) The gain factor of the estimate $\mathcal{R}$ as a function of ϕ. The flat lines are from the QCRBs, and the others are the CCRBs from the measurement. In figures (a), (b), and (d), the blue curves are for uniform temperature, $T_1 = T_2 = 300$ K, and red curves are for nonuniform temperatures, $T_1 = 400$ K and $T_2 = 200$ K. The source size is $a = 4$ km. The average temperature in all figures is $\bar{T} = 300$ K and $\mu = 0.5$.

unitary that diagonalizes each SLD is found as

$$\mathbf{U}_i = \frac{1}{\sqrt{2}}\begin{bmatrix} 1 & e^{i\phi_i} \\ 1 & -e^{i\phi_i} \end{bmatrix}. \tag{26}$$

Since the unitary is parametrized with a single parameter, we can drop the index i and find the ϕ that gives the most informative bound for joint estimation of both T_1 and T_2. In Fig. 2(a), we plot the diagonal elements of the classical Fisher information (CFI) matrix in Eq. (18) as a function of ϕ. If T_1 (dashed) and T_2 (solid) are equal, $T_1 = T_2$ (blue lines), a diagonal element $\mathcal{F}_1$ or $\mathcal{F}_2$ can be obtained by mirroring the other with respect to $\phi = \pi/2$. For different temperatures, $T_1 > T_2$ (red lines), the CFI matrix elements are not symmetric anymore. We observe that $\max(\mathcal{F}_1) > \max(\mathcal{F}_2)$, and their difference is related to temperature changes, which means that we can estimate the pixel with higher temperature better. We keep the average temperature ($\bar{T}$) constant. In both cases, we have the maximum value of CFI matrix elements $\max(\mathcal{F}_1) = \max(\mathcal{F}_2)$ at different ϕ and diagonalize the SLD for each parameter for single parameter estimation.

In Fig. 2(b), we plot $\mathrm{Tr}(F^{-1})/(\bar{T}^2)$ as a function of ϕ for $T_1 = T_2$ (blue) and $T_1 > T_2$ (red) temperature configurations. The scalar QCRBs are given by solid blue ($T_1 = T_2$) and dotted red ($T_1 > T_2$) flat lines, respectively. We see that for $T_1 = T_2$ (dot-dashed blue curve), we have the minimum of the scalar CCRB at $\phi = 0.5\pi$, and for $T_1 > T_2$ (dashed red curve), the minimum value is slightly shifted to the left. In both cases, the QCRBs are saturated. We see that the magnitudes of scalar QCRBs for $T_1 = T_2$ and $T_1 > T_2$ are close to each other if we keep the same $\bar{T}$ in both configurations. We also observe that $\mathrm{Tr}(\mathcal{F}^{-1})/(\bar{T}^2)$ for $T_1 > T_2$ (dashed red curve) at $\phi = \pi/2$ is still close to the QCRB (red dotted flat line). Even though to saturate the QCRB, ϕ must depend on the temperatures of all pixels, one can find the ϕ for $T_1 = T_2 = \bar{T}$ and use it to estimate different temperature configurations ($T_1 > T_2$).

In Fig. 2(c), we compare the most informative bound for optimal ϕ with the CCRB of local measurement (i.e., $\mathbf{U} = \mathbb{I}$) for joint estimation of T_1 and T_2 for a single measurement. We see that the dimensionless CCRB for the local measurement (green dashed line) goes to ∞ when the two sources have the same temperature. For a temperature difference around $\approx$10 K, it is around $\approx 10^6$, which is almost $\approx 10^4$ times larger than for an optimal nonlocal measurement using $\mathbf{U}_{\mathrm{opt}}$ (red dotted line). We also see that the optimal unitary saturates the QCRBs (solid black line). The bounds given in Fig. 2 are for a single measurement ($N = 1$) and reduced by a factor N for N independent measurements.

One can wonder what is the advantage of joint estimation of parameters over single parameter estimation. To answer that question, we can define the gain factor of the joint estimate [92,93]:

$$\mathcal{R} = p\sum_{i}^{p}\frac{1/F_{ii}}{\mathrm{Tr}\,(F^{-1})}, \tag{27}$$

where p is the total number of the parameters we want to estimate. The F stands for both the QFI matrix $\mathscr{F}$ and the CFI matrix $\mathcal{F}$. The gain factor $\mathcal{R}$ is upper bounded by p ($0 < \mathcal{R} \leqslant p$), where the factor p arises from the fact that for p single parameter estimations, the number of samples available for each parameter is reduced by a factor p compared to the total sample size, as different optimal measurements are typically required for different parameters. Since we have only two parameters to estimate (T_1 and T_2), the upper bound of the gain factor becomes $\mathcal{R} \leqslant 2$. If the gain factor is smaller than 1, $\mathcal{R} < 1$, then we do not have any advantage from joint estimation. In Fig. 2(d), we show the gain factor $\mathcal{R}$ of the estimation as a function of ϕ. It is close to 2 for the scalar QCRBs of $T_1 = T_2$ (solid blue) and $T_1 > T_2$ (dotted red straight lines). Furthermore, this advantage is achieved by the optimized unitary for CCRBs of $T_1 = T_2$ (dot-dashed blue curve) and $T_1 > T_2$ (dashed red curve). We have almost twice the advantage compared to single parameter estimation.

B. Resolution of a 1D array of pixel sources

We next consider a 1D array of pixels aligned parallel to the detector modes on the $\hat{x}$ axis ($p_x = n_x$ and $p_y = n_y = 1$). The size a of a pixel is the same for all pixels, and the separation between the two nearest pixels vanishes. The central position of each pixel is given by $\tilde{x}_j = (2j - p_x - 1)a/2$, and the position of detector k is $x_k = (2k - n_x - 1)\Delta x_{\max}/n_x$, where $j \in \{1, \dots, p_x\}$ and $k \in \{1, \dots, n_x\}$. The parameters that we want to estimate are the temperatures of each pixel given by a vector $\boldsymbol{\theta} = \{T_1, T_2, \dots, T_{p_x}\}$.

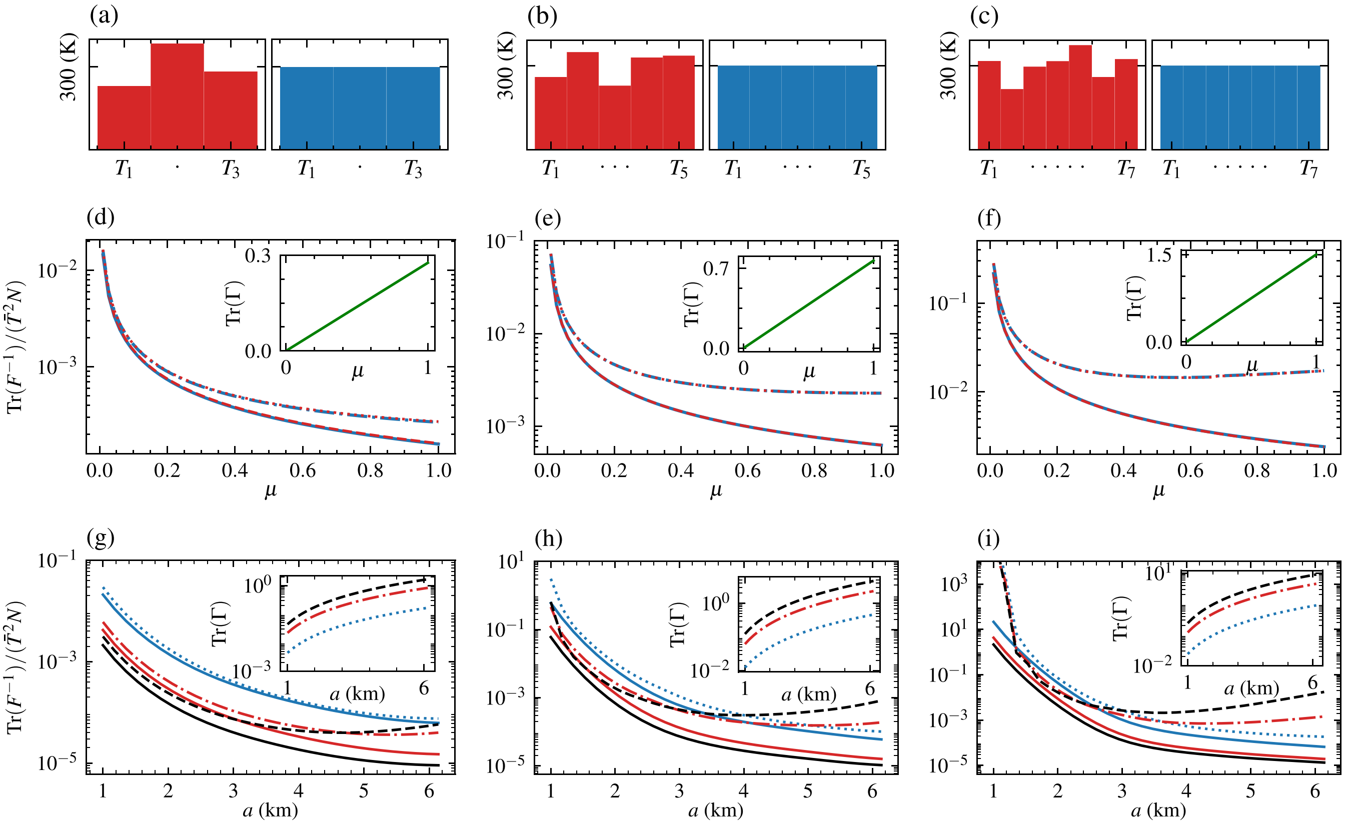

FIG. 3. (a)–(c) The temperature distribution of the 1D pixels with uniform temperature (blue bars) and different temperatures (red bars) for three, five, and seven pixels of the sources from (a) to (c), respectively. (d)–(f) The scalar CRBs (dimensionless) as a function of μ for the number of source pixels corresponding to (a)–(c). The solid blue and dashed red curves describe the QCRBs, and dotted red curves and dashed dotted blue curves describe the CCRBs for uniform and random temperature configurations. The insets show the total photon number as a function of μ with a solid green line. The pixel size for (d)–(f) is 2.5 km. (g)–(i) The scalar CRBs as a function of the source size a. The blue, red, and black lines correspond to different $\mu = (0.1, 0.5, 1.0)$, respectively. The solid lines represent the QCRBs, and dashed, dash-dotted, and dotted lines represent the scalar CCRBs of single-photon measurements with optimized unitary specific to different pixel configurations. The insets show the total photon number in the detector as a function of pixel size a, with the corresponding color of different μ. The average temperatures are assumed to be $\bar{T} = 300$ K, and the sample size is set to be $N = 10^6$.

The unitary $\mathbf{U}$ becomes a $n_x \times n_x$ matrix, and we need n_x^2 real parameters. Varying all the parameters of $\mathbf{U}$ independently to find a minimum for our cost function is a difficult task. Therefore, for $n > 2$, we use the steepest decent algorithm to minimize the most informative bound in Eq. (19). An efficient algorithm to minimize a given cost function with an argument of the Lie group of unitary matrices $U(n)$ is proposed in Ref. [94]. The unitary group $U(n)$ is a real Lie group of dimension n^2. In each iteration step, the conjugate gradient (CG) algorithm moves towards a minimum along the geodesic on the Riemannian manifold, corresponding to a straight line in Euclidean space. We explain the details of the CG algorithm adapted from Refs. [94–97] in the Appendix. These types of algorithms are widely used in classical communication systems. This paper uses the algorithm to optimize the POVM to achieve the quantum limit for imaging in passive remote sensing. We verified numerically that for our choice of the parameter set, the SLDs for different parameters commute on average over the corresponding quantum state for the n-mode interferometer.

In Fig. 3, we analyze the QCRB and the CCRB for different numbers of source pixels p_x (3, 5, and 7). The average temperatures are fixed to $\bar{T} = 300$ K for both random temperature distributions (left, red bars) and the uniform temperature distribution of the pixel sources (right, blue bars). From Figs. 3(d)–3(f), we show how the classical bounds from our measurement with optimized unitary change as a function of μ; insets show the changes of the corresponding total photon numbers as a function of μ in each configuration. Since the total mean photon number of the detection modes (solid green lines) decreases with μ and tends to $\mathrm{Tr}(\Gamma) \ll 1$, the POVMs of single-photon detections (red dotted and blue dash-dotted) saturate the QCRBs (red dashed and solid blue) for different and uniform temperature configurations, respectively. When $\mathrm{Tr}(\Gamma)$ gets close to 1, we see that the gap between the QCRB and the CCRB for single-photon measurement with optimized unitary ($\mathbf{U}_{\mathrm{opt}}$) increases. Additionally, the QCRBs decrease as the number of photons increases with μ, which means more photons from each pixel increase the QFI of the parameters. Thus, one needs to perform photon-number measurements rather than just single-photon ones to achieve the QCRB in this limit. Increasing the number of pixels p increases the total photon number on the interferometer. Thus the gap between the QCRBs and the CCRBs for measurement with optimized $\mathbf{U}_{\text{opt}}$ in each figure from Fig. 3(d) to Fig. 3(f) increases.

In Figs. 3(g)–3(i), we compare how both bounds change as a function of source size a for different temperature configurations. The black, red, and blue solid lines provide the QCRBs, and dashed black, dot-dashed red, and dotted blue provide the CRBs for single-photon POVMs measurement for different μ (0.1, 0.5, 1.0), respectively. Further, the insets provide the total photon numbers in the detection modes. We observe that the blue dotted lines ($\mu = 0.1$) are very close to the quantum limit and almost saturate the QCRBs for each source configuration for different source sizes. Once we increase μ, the gap between the two bounds increases as a function of source size a due to the increased number of photons. For instance, compare the gap for black dashed lines ($\mu = 1.0$) and blue dotted lines ($\mu = 0.1$). This is due to the limitation of the single-photon statistics for sources with a total photon number greater than 1 [$\text{Tr}(\Gamma) > 1$].

In general, the optimal unitary depends on the parameters (temperature distributions) we want to estimate. However, in real-life cases, we need to gain knowledge of the parameters to optimize the unitary completely. As we discuss in the section on two-pixel sources, a unitary for uniform temperature distributions can also be used to estimate different temperatures with the same $\bar{T}$ value. Experimentally, one can estimate the average temperature separately and construct the optimized unitary for the uniform temperature distribution ($\mathbf{U}_{\text{opt}}^{\text{uniform}}$). One then uses it to estimate the actual nonuniform temperature distribution. Further, we examine how both bounds change as a function of the number of pixels (p_x). In Fig. 4, we show the CCRBs for different $\mu = (0.05, 0.1, 0.5, 1.0)$ in Figs. 4(a)–4(d), respectively. The blue circles represent the initial random unitary for the CG algorithm. The black triangles are the scalar QCRBs. The red upward wedges are the scalar CCRBs from the optimized unitary ($\mathbf{U}_{\text{opt}}^{\text{image}}$) specific to random temperature distributions of pixels. Further, the green downward wedges are for the optimized unitary for uniform temperature distributions ($\mathbf{U}_{\text{opt}}^{\text{uniform}}$) of the pixels, used to estimate the corresponding random unitary temperature distributions with the same pixel number and the same average temperatures. The bounds from $\mathbf{U}_{\text{opt}}^{\text{uniform}}$ (green wedges) and $\mathbf{U}_{\text{opt}}^{\text{image}}$ (red wedges) are very close to each other in this logarithmic scale. Also, both almost saturate the QCRBs for $\mu = 0.05$ and 0.1 for different p_x. When we raise the number of pixels (p_x), we see that all bounds increase. Moreover, the gap between QCRBs and CCRBs from single-photon measurements becomes more significant for $\mu = 0.5$ and 1.0 compared to $\mu = 0.1$.

C. Resolution of 2D sources

This section considers an image with a total number of pixels $p = p_x p_y$ on the image plane. The number n of the modes of the 2D array interferometers will be considered the same as p, with $n = n_x n_y$. The size of each pixel is set to $a = 3$ km, which is around ten times smaller than the spatial resolution of SMOS considering the van Cittert–Zernike theorem, and the separation between the two nearest pixels is again set to zero. The parameters that we want to estimate are the temperatures of the 2D image $\boldsymbol{\theta} = \{T_1, T_2, \ldots, T_p\}$. We consider the case of drastic photon losses and set $\mu = 0.01$, which for $\bar{T} \approx 293$ K gives the total photon number around $\text{Tr}(\Gamma) \simeq 0.39$. In Fig. 5(a), we consider an actual image of $\hbar$ using 30 pixels on the image plane and a 30-mode interferometer on the source plane. The unitary optimized ($\mathbf{U}_{\text{opt}}^{\text{image}}$) for this image or the unitary for a uniform temperatures distribution ($\mathbf{U}_{\text{opt}}^{\text{uniform}}$) is applied in the preprocessing stage to estimate the parameters. For the classical measurement, we consider a local measurement scenario with $\mathbf{U} = \mathbb{I}$. Further, the image from different measurement strategies is reconstructed by using a maximum likelihood estimator for a sample of size N. In Fig. 5(b), we reconstructed the image by using $\mathbf{U}_{\text{opt}}^{\text{image}}$. We have the advantage of the nonlocal measurement and the optimized unitary specific to the image. The reconstructed image is close to the actual image for this parameter regime. Though this unitary depends on the parameter set, we estimate that the same resolution limit may be achieved using adaptive types of measurement [98] by iteratively updating the unitary for each sample after measurement.

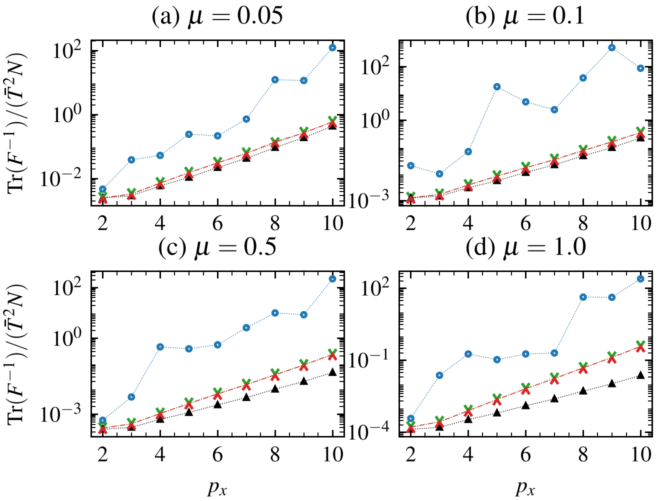

FIG. 4. (a)–(d) The scalar CRBs (dimensionless) for different numbers of pixels p_x along the $\hat{x}$ axis in a 1D array and $\mu = (0.05, 0.1, 0.5, 1.0)$, respectively. The black triangles represent QCRBs, and red upward wedges represent the scalar CCRBs that we get using the optimized unitary $\mathbf{U}_{\text{opt}}^{\text{image}}$ specific to the actual temperature distributions of source pixels. Green downward wedges are for the unitary $\mathbf{U}_{\text{opt}}^{\text{uniform}}$ optimized for the uniform temperature of the pixels used to estimate the actual temperature distribution with the same average temperature. Blue circles correspond to scalar CRBs for the initial random unitary before optimization. Pixel size is $a = 2.5$ km, average temperature $\bar{T} = 300$ K, and sample size $N = 10^6$.

However, this is beyond the scope of this paper. On the other hand, for easy experimental realization, we reconstruct the image by using $\mathbf{U}_{\text{opt}}^{\text{uniform}}$ in Fig. 5(c). One can independently estimate the average temperature from the source distribution and construct this general unitary for any image. As we see, the reconstructed image still reveals the actual image nicely, but as expected, it is not as sharp as the image from a specifically optimized unitary. We reconstructed the image from local measurement in Fig. 5(d). Clearly, this reconstructed image is not close to the original one. This is

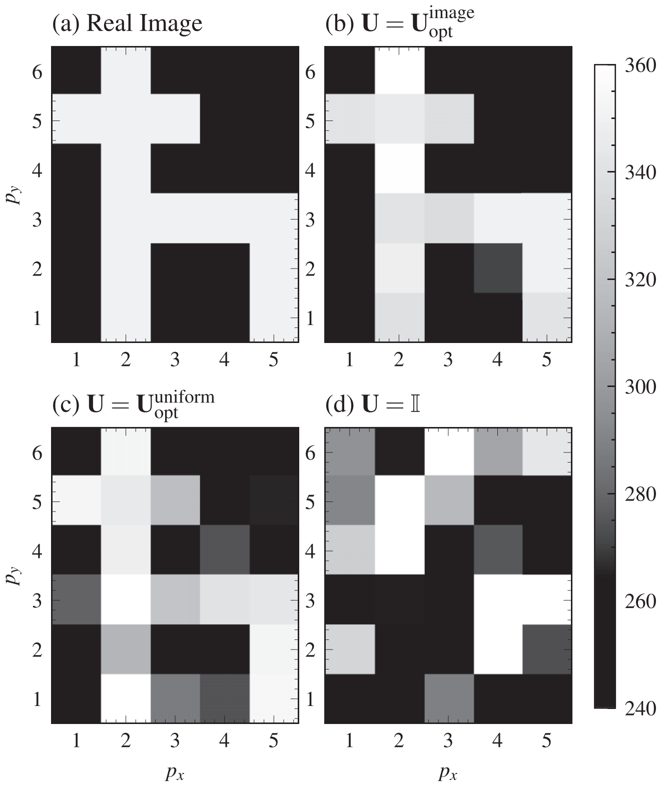

FIG. 5. (a) The image on the source plane with 30 pixels will be estimated using a maximum likelihood estimator. (b) The reconstructed image after single-photon detection in detection modes $\hat{d}_i$ obtained from using the optimized unitary $\mathbf{U}_{\text{opt}}^{\text{image}}$ specific to the temperature distribution. (c) The reconstructed image using a unitary optimized for uniform temperature distribution $\mathbf{U}_{\text{opt}}^{\text{uniform}}$. (d) The reconstructed image using a local measurement of single photons considering $\mathbf{U} = \mathbb{I}$. Pixel size $a = 3.0$ km, average temperature $\bar{T} \approx 293$ K, and sample size $N = 10^8$.

expected for our pixel size $a = 3$ km, well below the limit of the Rayleigh resolution for SMOS, which is around 35 km, based on the van Cittert–Zernike theorem [48–51].

IV. CONCLUSION

In summary, we formulated passive remote sensing as a quantum multiparameter estimation problem, where we focused on the temperatures on the ground as parameters rather than geometrical information of sources that are currently at the center of attention in quantum imaging, such as the separation, centroid, or phases of sources. An antenna array with as many antennas as desired pixels in the source plane receives thermal electromagnetic radiation in receiver modes that are then mixed according to an optimized unitary transformation. Single-photon detectors detect the photons in the corresponding optimized detection modes. The function to be optimized is a scalar classical Cramér-Rao bound obtained by contracting the inverse Fisher information matrix for estimating the temperatures from the photon-counting results with a positive weight matrix. With the latter one we can give different preferences for high resolution to different parts of the image. The optimization of the bound over all unitary mode mixings leads to a “most-informative bound [55].” For a uniform weight over all pixels, we show that with this procedure, one can, in the case of the Gaussian white-noise characteristic of thermal states, approximatively saturate the scalar quantum Cramér-Rao bound based on the contraction of the quantum Fisher information matrix for the multiparameter estimation problem with the same positive weight matrix (chosen as the identity in the present paper). In principle, the optimized unitary depends on the actual temperature distribution, but we showed that the unitary obtained from a uniform temperature distribution gives still much better resolution than direct photon counting in the incoming modes. For the optimization over the unitaries, we used a conjugate gradient algorithm. We showed that the found optimal mode of mixing, followed by single-photon detection, leads to a spatial resolution of the reconstructed images that are at least about an order of magnitude better than Rayleigh’s limit (about 3 km instead of 35 km for an antenna array comparable with the

Algorithm 1. Conjugate gradient algorithm for unitary optimization

```
Require: $k = 0$, $\mathbf{U}_k$ = Random Unitary, $n = \mathbf{dim}(\mathbf{U}_k)$, $\alpha = 1$
while $k \neq k_{\max}$ do
    if $k$ modulo $n^2 = 0$ then
        $\mathbf{G}_k = \frac{\partial}{\partial \mathbf{U}^*} F(\mathbf{U}_k)$
        $\mathbf{W}_k = \mathbf{G}_k \mathbf{U}_k^\dagger - \mathbf{U}_k \mathbf{G}_k^\dagger$
        $\mathbf{H}_k := \mathbf{W}_k$
    else
        $\mathbf{W}_k \leftarrow \mathbf{W}_{k+1}$
        $\mathbf{H}_k \leftarrow \mathbf{H}_{k+1}$
    end if

    $\mathbf{P}_k = \exp(-\alpha \mathbf{H}_k)$
    $\mathbf{Q}_k = \mathbf{P}_k \mathbf{P}_k$

    while $F(\mathbf{U}_k) - F(\mathbf{Q}_k \mathbf{U}_k) \geq \alpha \langle \mathbf{W}_k, \mathbf{H}_k \rangle$ do
        $\mathbf{P}_k = \mathbf{Q}_k$
        $\mathbf{Q}_k = \mathbf{P}_k \mathbf{P}_k$
        $\alpha = 2\mu$
    end while

    while $F(\mathbf{U}_k) - F(\mathbf{P}_k \mathbf{U}_k) < (\alpha/2) \langle \mathbf{W}_k, \mathbf{H}_k \rangle$ do
        $\alpha = \alpha/2$
        $\mathbf{P}_k = \exp(-\alpha \mathbf{H}_k)$
    end while

    $\mathbf{U}_{k+1} = \mathbf{P}_k \mathbf{U}_k$
    $\mathbf{G}_{k+1} = \frac{\partial}{\partial \mathbf{U}^*} F(\mathbf{U}_{k+1})$
    $\mathbf{W}_{k+1} = \mathbf{G}_{k+1} \mathbf{U}_{k+1}^\dagger - \mathbf{U}_{k+1} \mathbf{G}_{k+1}^\dagger$

    $\gamma_k := \frac{\langle \mathbf{W}_{k+1} - \mathbf{W}_k, \mathbf{W}_k \rangle}{\langle \mathbf{W}_k, \mathbf{W}_k \rangle}$
    $\mathbf{H}_{k+1} = \mathbf{W}_{k+1} + \gamma_k \mathbf{H}_k$

    if $\langle \mathbf{W}_{k+1}, \mathbf{H}_{k+1} \rangle \leq 0$ then
        $\mathbf{H}_{k+1} = \mathbf{W}_{k+1}$
    end if

    $\mathbf{U}_k \leftarrow \mathbf{U}_{k+1}$
    $k \leftarrow k + 1$
end while
```

one of SMOS, even for substantial photon losses), given in the present case by the van Cittert–Zernike theorem. The optimal unitary can be decomposed into $SU(2)$ group elements using beam splitters and phase shifters and can be realized as linear optical quantum computing. Given the recent availability of single-photon detection in the microwave domain, our results show a path towards substantially enhanced resolution in passive remote sensing compared to classical interferometers that essentially implement homodyne quadrature measurements. Further improvements might be possible for larger photon numbers or smaller losses if photon-number resolved measurements are available.

ACKNOWLEDGMENTS

D.B. and E.K. are grateful for support by Deutsche Forschungsgemeinschaft Project No. BR 52213-1. We thank Gerardo Adesso for discussions, and D.B. thanks Yann Kerr, Bernard Rougé, and the entire SMOS team in Toulouse for valuable insights into that mission.

APPENDIX: CONJUGATE GRADIENT ALGORITHM FOR OPTIMIZATION

This section summarizes a practical CG algorithm given by Refs. [94,96,97]. The generic CG algorithm starts with ($k = 0$) finding the conjugate gradient $\mathbf{G}_k$ of the cost function $F(\mathbf{U}_k)$ for an initial unitary matrix, where

$$\mathbf{G}_k = \frac{\partial}{\partial \mathbf{U}^*} F(\mathbf{U}_k). \tag{A1}$$

Then, the Riemannian gradient $\mathbf{W}_k$ at that point can be found by

$$\mathbf{W}_k = \mathbf{G}_k \mathbf{U}_k^\dagger - \mathbf{U}_k \mathbf{G}_k^\dagger. \tag{A2}$$

By determining the step size α using the Armijo method (see Ref. [95]) along the geodesic direction (in the direction of $-\mathbf{H}_k$), one can update the unitary by

$$\mathbf{U}_{k+1} = \exp(-\alpha \mathbf{H}_k)\mathbf{U}_k. \tag{A3}$$

Further, the new search direction can be found by using the Polak-Ribierre formula $\mathbf{H}_{k+1} = \mathbf{W}_{k+1} + \boldsymbol{\gamma}_k \mathbf{H}_k$, where

$$\boldsymbol{\gamma}_k := \frac{\langle \mathbf{W}_{k+1} - \mathbf{W}_k, \mathbf{W}_k \rangle}{\langle \mathbf{W}_k, \mathbf{W}_k \rangle}. \tag{A4}$$

The inner product defined as $\langle X, Y \rangle \equiv \mathrm{Tr}(X^\dagger Y)/2$ induces a bi-invariant metric on the unitary group $U(n)$. We reset the search direction periodically to ensure the direction of $\mathbf{H}_k$ is a descent direction. Then the next iteration continues accordingly (see pseudocode in Algorithm 1). The algorithm runs until it converges to a minimum value of the cost function or a maximum number of iterations k_{max}. To efficiently deal with the gradient of the cost functions, we used the PYTORCH gradient function. PYTORCH is used in machine learning for its GPU capabilities.

---

[1] A. Bhandari, A. Kadambi, and R. Raskar, *Computational Imaging* (MIT, Cambridge, MA, 2022).

[2] R. Hanbury Brown and R. Q. Twiss, A test of a new type of stellar interferometer on sirius, Nature (London) **178**, 1046 (1956).

[3] U. Fano, Quantum theory of interference effects in the mixing of light from phase-independent sources, Am. J. Phys. **29**, 539 (1961).

[4] S. W. Hell and J. Wichmann, Breaking the diffraction resolution limit by stimulated emission: Stimulated-emission-depletion fluorescence microscopy, Opt. Lett. **19**, 780 (1994).

[5] S. W. Hell, Far-field optical nanoscopy, Science **316**, 1153 (2007).

[6] C. W. Helstrom, Detection theory and quantum mechanics, Inform. Comput. **10**, 254 (1967).

[7] C. W. Helstrom, Quantum detection and estimation theory, J. Stat. Phys. **1**, 231 (1969).

[8] C. W. Helstrom, Cramer-Rao inequalities for operator-valued measures in quantum mechanics, Int. J. Theor. Phys. **8**, 361 (1973).

[9] C. W. Helstrom, Estimation of object parameters by a quantum-limited optical system, J. Opt. Soc. Am. **60**, 233 (1970).

[10] O. Pinel, J. Fade, D. Braun, P. Jian, N. Treps, and C. Fabre, Ultimate sensitivity of precision measurements with intense Gaussian quantum light: A multimodal approach, Phys. Rev. A **85**, 010101(R) (2012).

[11] O. Pinel, P. Jian, N. Treps, C. Fabre, and D. Braun, Quantum parameter estimation using general single-mode Gaussian states, Phys. Rev. A **88**, 040102(R) (2013).

[12] M. Tsang, Quantum limit to subdiffraction incoherent optical imaging, Phys. Rev. A **99**, 012305 (2019).

[13] S. Zhou and L. Jiang, Modern description of Rayleigh's criterion, Phys. Rev. A **99**, 013808 (2019).

[14] G. Sorelli, M. Gessner, M. Walschaers, and N. Treps, Moment-based superresolution: Formalism and applications, Phys. Rev. A **104**, 033515 (2021).

[15] J. Řehaček, Z. Hradil, B. Stoklasa, M. Paúr, J. Grover, A. Krzic, and L. L. Sánchez-Soto, Multiparameter quantum metrology of incoherent point sources: Towards realistic superresolution, Phys. Rev. A **96**, 062107 (2017).

[16] C. Napoli, S. Piano, R. Leach, G. Adesso, and T. Tufarelli, Towards Superresolution Surface Metrology: Quantum Estimation of Angular and Axial Separations, Phys. Rev. Lett. **122**, 140505 (2019).

[17] R. Nair and M. Tsang, Far-Field Superresolution of Thermal Electromagnetic Sources at the Quantum Limit, Phys. Rev. Lett. **117**, 190801 (2016).

[18] C. Lupo and S. Pirandola, Ultimate Precision Bound of Quantum and Subwavelength Imaging, Phys. Rev. Lett. **117**, 190802 (2016).

[19] W. Larson and B. E. A. Saleh, Resurgence of Rayleigh's curse in the presence of partial coherence, Optica **5**, 1382 (2018).

[20] S. Kurdziałek and R. Demkowicz-Dobrzański, Super-resolution optical fluctuation imaging: Fundamental estimation theory perspective, J. Opt. **23**, 075701 (2021).

[21] M. I. Kolobov and C. Fabre, Quantum Limits on Optical Resolution, Phys. Rev. Lett. **85**, 3789 (2000).

[22] S. Z. Ang, R. Nair, and M. Tsang, Quantum limit for two-dimensional resolution of two incoherent optical point sources, Phys. Rev. A **95**, 063847 (2017).

[23] M. Tsang, Quantum Nonlocality in Weak-Thermal-Light Interferometry, Phys. Rev. Lett. **107**, 270402 (2011).

[24] E. Bisketzi, D. Branford, and A. Datta, Quantum limits of localisation microscopy, New J. Phys. **21**, 123032 (2019).

[25] M. Bojer, Z. Huang, S. Karl, S. Richter, P. Kok, and J. von Zanthier, A quantitative comparison of amplitude versus intensity interferometry for astronomy, New J. Phys. **24**, 043026 (2021).

[26] C. Datta, M. Jarzyna, Y. L. Len, K. Łukanowski, J. Kołodyński, and K. Banaszek, Sub-Rayleigh resolution of two incoherent sources by array homodyning, Phys. Rev. A **102**, 063526 (2020).

[27] J. O. de Almeida, J. Kołodyński, C. Hirche, M. Lewenstein, and M. Skotiniotis, Discrimination and estimation of incoherent sources under misalignment, Phys. Rev. A **103**, 022406 (2021).

[28] K. Liang, S. A. Wadood, and A. N. Vamivakas, Coherence effects on estimating general sub-rayleigh object distribution moments, Phys. Rev. A **104**, 022220 (2021).

[29] M. Tsang, Subdiffraction incoherent optical imaging via spatial-mode demultiplexing, New J. Phys. **19**, 023054 (2017).

[30] M. Tsang, Quantum limits to optical point-source localization, Optica **2**, 646 (2015).

[31] I. Karuseichyk, G. Sorelli, M. Walschaers, N. Treps, and M. Gessner, Resolving mutually-coherent point sources of light with arbitrary statistics, Phys. Rev. Res. **4**, 043010 (2022).

[32] C. Lupo, Z. Huang, and P. Kok, Quantum Limits to Incoherent Imaging are Achieved by Linear Interferometry, Phys. Rev. Lett. **124**, 080503 (2020).

[33] D. Gottesman, T. Jennewein, and S. Croke, Longer-Baseline Telescopes Using Quantum Repeaters, Phys. Rev. Lett. **109**, 070503 (2012).

[34] E. T. Khabiboulline, J. Borregaard, K. De Greve, and M. D. Lukin, Optical Interferometry with Quantum Networks, Phys. Rev. Lett. **123**, 070504 (2019).

[35] Y. Wang, Y. Zhang, and V. O. Lorenz, Superresolution in interferometric imaging of strong thermal sources, Phys. Rev. A **104**, 022613 (2021).

[36] C. Datta, Y. L. Len, K. Łukanowski, K. Banaszek, and M. Jarzyna, Sub-Rayleigh characterization of a binary source by spatially demultiplexed coherent detection, Opt. Express **29**, 35592 (2021).

[37] M. P. Backlund, Y. Shechtman, and R. L. Walsworth, Fundamental Precision Bounds for Three-Dimensional Optical Localization Microscopy with Poisson Statistics, Phys. Rev. Lett. **121**, 023904 (2018).

[38] M. Mazelanik, A. Leszczynski, and M. Parniak, Optical-domain spectral super-resolution enabled by a quantum memory, Nat. Commun. **13**, 691 (2021).

[39] M. Paúr, B. Stoklasa, Z. Hradil, L. L. Sánchez-Soto, and J. Rehacek, Achieving the ultimate optical resolution, Optica **3**, 1144 (2016).

[40] A. A. Pushkina, G. Maltese, J. I. Costa-Filho, P. Patel, and A. I. Lvovsky, Super-Resolution Linear Optical Imaging in the Far Field Phys. Rev. Lett. **127**, 253602 (2021).

[41] P. Boucher, C. Fabre, G. Labroille, and N. Treps, Spatial optical mode demultiplexing as a practical tool for optimal transverse distance estimation, Optica **7**, 1621 (2020).

[42] G. Sorelli, M. Gessner, M. Walschaers, and N. Treps, Optimal Observables and Estimators for Practical Superresolution Imaging, Phys. Rev. Lett. **127**, 123604 (2021).

[43] P. C. Humphreys, M. Barbieri, A. Datta, and I. A. Walmsley, Quantum Enhanced Multiple Phase Estimation, Phys. Rev. Lett. **111**, 070403 (2013).

[44] C. N. Gagatsos, D. Branford, and A. Datta, Gaussian systems for quantum-enhanced multiple phase estimation, Phys. Rev. A **94**, 042342 (2016).

[45] P. A. Knott, T. J. Proctor, A. J. Hayes, J. F. Ralph, P. Kok, and J. A. Dunningham, Local versus global strategies in multiparameter estimation, Phys. Rev. A **94**, 062312 (2016).

[46] L. Pezzè, M. A. Ciampini, N. Spagnolo, P. C. Humphreys, A. Datta, I. A. Walmsley, M. Barbieri, F. Sciarrino, and A. Smerzi, Optimal Measurements for Simultaneous Quantum Estimation of Multiple Phases, Phys. Rev. Lett. **119**, 130504 (2017).

[47] E. Köse, G. Adesso, and D. Braun, Quantum-enhanced passive remote sensing, Phys. Rev. A **106**, 012601 (2022).

[48] E. Anterrieu, A resolving matrix approach for synthetic aperture imaging radiometers, IEEE Trans. Geosci. Remote Sens. **42**, 1649 (2004).

[49] I. Corbella, N. Duffo, M. Vall-llossera, A. Camps, and F. Torres, The visibility function in interferometric aperture synthesis radiometry, IEEE Trans. Geosci. Remote Sens. **42**, 1677 (2004).

[50] D. Le Vine, Synthetic aperture radiometer systems, IEEE Trans. Microwave Theory Techn. **47**, 2228 (1999).

[51] A. R. Thompson, J. M. Moran, and George W. Swenson, Jr., *Interferometry and Synthesis in Radio Astronomy* (Springer, New York, 2017).

[52] P. van Cittert, Die wahrscheinliche schwingungsverteilung in einer von einer lichtquelle direkt oder mittels einer linse beleuchteten ebene, Physica **1**, 201 (1934).

[53] F. Zernike, The concept of degree of coherence and its application to optical problems, Physica **5**, 785 (1938).

[54] D. Braun, Y. Monjid, B. Rougé, and Y. Kerr, Generalization of the Van Cittert–Zernike theorem: Observers moving with respect to sources, Meas. Sci. Technol. **27**, 015002 (2016).

[55] F. Albarelli, M. Barbieri, M. Genoni, and I. Gianani, A perspective on multiparameter quantum metrology: From theoretical tools to applications in quantum imaging, Phys. Lett. A **384**, 126311 (2020).

[56] P. Kok, W. J. Munro, K. Nemoto, T. C. Ralph, J. P. Dowling, and G. J. Milburn, Linear optical quantum computing with photonic qubits, Rev. Mod. Phys. **79**, 135 (2007).

[57] T. Baumgratz and A. Datta, Quantum Enhanced Estimation of a Multidimensional Field, Phys. Rev. Lett. **116**, 030801 (2016).

[58] E. Bagan, M. A. Ballester, R. D. Gill, A. Monras, and R. Muñoz-Tapia, Optimal full estimation of qubit mixed states, Phys. Rev. A **73**, 032301 (2006).

[59] M. Guta and J. Kiukas, Information geometry and local asymptotic normality for multi-parameter estimation of quantum Markov dynamics, J. Math. Phys. **58**, 052201 (2017).

[60] M. Szczykulska, T. Baumgratz, and A. Datta, Multi-parameter quantum metrology, Adv. Phys.: X **1**, 621 (2016).

[61] S. Ragy, M. Jarzyna, and R. Demkowicz-Dobrzański, Compatibility in multiparameter quantum metrology, Phys. Rev. A **94**, 052108 (2016).

[62] D. Braun, Y. Monjid, B. Rougé, and Y. Kerr, Fourier-correlation imaging, J. Appl. Phys. **123**, 074502 (2018).

[63] J. Liu, H. Yuan, X.-M. Lu, and X. Wang, Quantum Fisher information matrix and multiparameter estimation, J. Phys. A: Math. Theor. **53**, 023001 (2020).

[64] J. Shapiro, The quantum theory of optical communications, IEEE J. Sel. Top. Quantum Electron. **15**, 1547 (2009).

[65] C. Oh, S. Zhou, Y. Wong, and L. Jiang, Quantum Limits of Superresolution in a Noisy Environment, Phys. Rev. Lett. **126**, 120502 (2021).

[66] M. Gessner, C. Fabre, and N. Treps, Superresolution Limits from Measurement Crosstalk, Phys. Rev. Lett. **125**, 100501 (2020).

[67] Y. L. Len, C. Datta, M. Parniak, and K. Banaszek, Resolution limits of spatial mode demultiplexing with noisy detection, Int. J. Quantum. Inform. **18**, 1941015 (2020).

[68] K. J. Blow, R. Loudon, S. J. D. Phoenix, and T. J. Shepherd, Continuum fields in quantum optics, Phys. Rev. A **42**, 4102 (1990).

[69] L. Mandel, and E. Wolf, *Optical Coherence and Quantum Optics* (Cambridge University Press, Cambridge, 1995).

[70] R. J. Glauber, Coherent and incoherent states of the radiation field, Phys. Rev. **131**, 2766 (1963).

[71] M. O. Scully, and M. S. Zubairy, *Quantum Optics* (Cambridge University Press, Cambridge, 1997).

[72] R. Loudon and T. von Foerster, The quantum theory of light, Am. J. Phys. **42**, 1041 (1974).

[73] R. Kubo, The fluctuation-dissipation theorem, Rep. Prog. Phys. **29**, 255 (1966).

[74] S. Savasta, O. Di Stefano, and R. Girlanda, Light quantization for arbitrary scattering systems, Phys. Rev. A **65**, 043801 (2002).

[75] E. A. Sharkov, *Passive Microwave Remote Sensing of the Earth: Physical Foundations* (Springer-Verlag, Berlin, 2011).

[76] L. D. Landau, and E. M. Lifshits, *Statistical Physics* (Elsevier Science, 1980), Vol. 5.

[77] R. Carminati and J.-J. Greffet, Near-Field Effects in Spatial Coherence of Thermal Sources, Phys. Rev. Lett. **82**, 1660 (1999).

[78] J. Zmuidzinas, Cramér–Rao sensitivity limits for astronomical instruments: Implications for interferometer design, J. Opt. Soc. Am. A **20**, 218 (2003).

[79] J. Zmuidzinas, Thermal noise and correlations in photon detection, Appl. Opt. **42**, 4989 (2003).

[80] J. S. Sidhu and P. Kok, Geometric perspective on quantum parameter estimation, AVS Quantum Sci. **2**, 014701 (2020).

[81] Y. Gao and H. Lee, Bounds on quantum multiple-parameter estimation with Gaussian state, Eur. Phys. J. D **68**, 347 (2014).

[82] D. Braun, P. Jian, O. Pinel, and N. Treps, Precision measurements with photon-subtracted or photon-added Gaussian states, Phys. Rev. A **90**, 013821 (2014).

[83] G. Adesso, S. Ragy, and A. R. Lee, Continuous variable quantum information: Gaussian states and beyond, Open Syst. Inf. Dyn. **21**, 1440001 (2014).

[84] S. Olivares, Quantum optics in the phase space: A tutorial on Gaussian states, Eur. Phys. J. Spec. Top. **203**, 3 (2012).

[85] C. Weedbrook, S. Pirandola, R. García-Patrón, N. J. Cerf, T. C. Ralph, J. H. Shapiro, and S. Lloyd, Gaussian quantum information, Rev. Mod. Phys. **84**, 621 (2012).

[86] S. L. Braunstein and C. M. Caves, Statistical distance and the geometry of quantum states, Phys. Rev. Lett. **72**, 3439 (1994).

[87] M. G. A. Paris, Quantum estimation for quantum technology, Int. J. Quantum. Inform. **07**, 125 (2009).

[88] A. Holevo, Statistical decision theory for quantum systems, J. Multivariate Anal. **3**, 337 (1973).

[89] M. Tsang, F. Albarelli, and A. Datta, Quantum Semiparametric Estimation, Phys. Rev. X **10**, 031023 (2020).

[90] I. J. Myung, Tutorial on maximum likelihood estimation, J. Math. Psychol. **47**, 90 (2003).

[91] M. Paris and J. Řeháček, *Quantum State Estimation* (Springer Berlin, Heidelberg, 2004).

[92] R. Nichols, P. Liuzzo-Scorpo, P. A. Knott, and G. Adesso, Multiparameter Gaussian quantum metrology, Phys. Rev. A **98**, 012114 (2018).

[93] R. Yousefjani, R. Nichols, S. Salimi, and G. Adesso, Estimating phase with a random generator: Strategies and resources in multiparameter quantum metrology, Phys. Rev. A **95**, 062307 (2017).

[94] T. Abrudan, J. Eriksson, and V. Koivunen, Conjugate gradient algorithm for optimization under unitary matrix constraint, Signal Process. **89**, 1704 (2009).

[95] T. Abrudan, J. Eriksson, and V. Koivunen, Efficient line search methods for Riemannian optimization under unitary matrix constraint, in *Proceedings of the 2007 Conference Record of the Forty-First Asilomar Conference on Signals, Systems and Computers* (IEEE, New York, 2007), pp. 671–675.

[96] T. E. Abrudan, J. Eriksson, and V. Koivunen, Steepest descent algorithms for optimization under unitary matrix constraint, IEEE Trans. Signal Process. **56**, 1134 (2008).

[97] T. Abrudan, J. Eriksson, and V. Koivunen, Efficient Riemannian algorithms for optimization under unitary matrix constraint, in *Proceedings of the 2008 IEEE International Conference on Acoustics, Speech and Signal Processing* (IEEE, New York, 2008), pp. 2353–2356.

[98] A. Fujiwara, Strong consistency and asymptotic efficiency for adaptive quantum estimation problems, J. Phys. A: Math. Theor. **44**, 079501 (2011).